Spatiotemporal dynamics of membrane surface charge regulates cell polarity and migration

Tatsat Banerjee[1,2], Debojyoti Biswas[3, ‡], Dhiman Sankar Pal[1, ‡], Yuchuan Miao[1,4], Pablo A. Iglesias[1,3], Peter N. Devreotes[1,4]*.

[1]Department of Cell Biology and Center for Cell Dynamics, School of Medicine, Johns Hopkins University, Baltimore, MD, USA.

[2]Department of Chemical and Biomolecular Engineering, Whiting School of Engineering, Johns Hopkins University, Baltimore, MD, USA.

[3]Department of Electrical and Computer Engineering, Whiting School of Engineering, Johns Hopkins University, Baltimore, MD, USA.

[4]Department of Biological Chemistry, School of Medicine, Johns Hopkins University, Baltimore, MD, USA.

‡These authors contributed equally.

*Email: pnd@jhmi.edu

SUPPLEMENTARY NOTE 1

Computational model

Excitable signal transduction system:

The excitable system consists of three states – F, B, and R[1]. The system dynamics can be described by the stochastic partial differential equations (SPDE) as follows:

$$\frac{\partial \mathrm{F}}{\partial \mathrm{t}} = -(\mathrm{a}_1 + \mathrm{a}_2\mathrm{R})\mathrm{F} + \left(\frac{\mathrm{a}_{30} + \mathrm{a}_3(\mathrm{Z}-\mathrm{W})}{\mathrm{a}_4^2 + \mathrm{B}^2} + \mathrm{a}_5\right)(\mathrm{F}_\mathrm{T} - \mathrm{F}) + \mathrm{D}_\mathrm{F}\nabla^2\mathrm{F} + \mathrm{w}_\mathrm{F} = P_F(\cdot) + \mathrm{D}_\mathrm{F}\nabla^2\mathrm{F} + \mathrm{w}_\mathrm{F}\,, \quad (1)$$

$$\frac{\partial \mathrm{B}}{\partial \mathrm{t}} = \mathrm{b}_1 - \mathrm{b}_2\mathrm{F}\mathrm{B} + \mathrm{D}_\mathrm{B}\nabla^2\mathrm{B} + \mathrm{w}_\mathrm{B} = P_B(\cdot) + \mathrm{D}_\mathrm{B}\nabla^2\mathrm{B} + \mathrm{w}_\mathrm{B}, \quad (2)$$

$$\frac{\partial \mathrm{R}}{\partial \mathrm{t}} = -\mathrm{c}_1\mathrm{R} + \mathrm{c}_2\mathrm{F}(\mathrm{R}_\mathrm{T} - \mathrm{R}) + \mathrm{D}_\mathrm{R}\nabla^2\mathrm{F} + \mathrm{w}_\mathrm{R} = P_R(\cdot) + \mathrm{D}_\mathrm{R}\nabla^2\mathrm{R} + \mathrm{w}_\mathrm{R}, \quad (3)$$

where F_T, R_T are the total amount of F and R, respectively. The stochasticity affecting state X is introduced through the signal, w_X representing the white noise process with respective variance $\sigma_X{}^2 \propto P_X(\cdot)$. Eqn. (1-3) is the manifestation of the standard activator-inhibitor system where F is the fast activator and R is the slow inhibitor. The original auto catalytic loop around the activator is replaced by the mutual inhibitory interactions between F and B. First two reaction terms in Eqn. (1) represent the basal and R-dependent inactivation of F, respectively. The third reaction term represents the nonlinear activation with a negative feedback from B along with the positive feedback from the downstream polarity module (discussed later). The fourth term involves the linear basal activation rate. The reaction terms in Eqn. (2) involve basal activation and F-dependent deactivation of B, respectively. In the Eqn. (3), the reaction terms represent the deactivation and F-dependent activation of R. The total amounts of F and R are conserved in the system.

Polarity Mechanism:

To simulate the behavior of polar cells, we coupled the excitable system with a two-component biasing network based on the local excitation and global inhibition (LEGI) principle [2]:

$$\frac{\partial Z}{\partial t} = k(R - Z) + D_Z \nabla^2 Z + w_4, \qquad (4)$$

$$\frac{\partial W}{\partial t} = \varepsilon_w k(R - W) + D_w \nabla^2 W + w_5, \qquad (5)$$

where Z is the fast, local activator and W is the slow ($\varepsilon_w < 1$), globally diffusing ($D_w \gg D_Z$) inhibitor. Both activator and the inhibitor of the polarity mechanism are activated by R of upstream excitable system. The output of this biasing network ($Z - W$) positively affects the nonlinear activation of F thus increasing the probability of firing at the former firing locations and resulting long lived patches of F activity.

Positively Charged Actuator Dynamics:

To model the partitioning of the uniformly recruited charge sensors on the membrane, we considered two populations of charge sensors – fast diffusing, C_{mf} and slow diffusing C_{mb} ($D_{C_{mf}^+} \gg D_{C_{mb}^+}$). The system dynamics assumed for the positive charge actuator (Opto-ACTU+) is given by,

$$\frac{\partial C_{mf}^+}{\partial t} = \varepsilon_L(d_1 L(x)\mathbb{I}_L(t) - d_2 C_{mf}^+) + d_3 F C_{mb}^+ - d_4 B C_{mf}^+ + D_{C_{mf}^+}\nabla^2 C_{mf}^+ + w_6, \quad (6)$$

$$\frac{\partial C_{mb}^+}{\partial t} = -d_3 F C_{mb}^+ + d_4 B C_{mf}^+ + D_{C_{mb}^+}\nabla^2 C_{mb}^+ + w_7. \quad (7)$$

The first term in Eqn. (6) represents the spatiotemporal recruitment of charge actuators to the membrane. The indicator function L(x) controls the spatial location(s) of the recruitment whereas $\mathbb{I}_L(t)$ controls the instant and the time span. The second term denotes the reverse process. The third and the fourth term of Eqn. (6) represent F and B-mediated interconversions of C_{mf}^+ and C_{mb}^+. The total positive charge actuators (C_m^+) on the membrane is given by, $C_m^+ = C_{mf}^+ + C_{mb}^+$. The effect of positive charge actuation on the membrane states is incorporated through a negative feedback term involving C_{mb}^+ in the B dynamics as follows:

$$\frac{\partial B}{\partial t} = b_1 - b_2 F B - b_3 C_{mb}^+ B + D_B \nabla^2 B + w_B.$$

Negatively Charged Actuator Dynamics:

For modeling negative charge actuators, we followed a similar methodology as discussed above. The system dynamics assumed for the negative charge actuator (Opto-ACTU–) is given by,

$$\frac{\partial C_{mf}^{-}}{\partial t} = d_1 L(x)\mathbb{I}_L(t) - d_2 C_{mf}^{-} + d_3 B C_{mb}^{-} - d_4 F C_{mf}^{-} + D_{C_{mf}^{-}} \nabla^2 C_{mf}^{-} + w_8, \quad (8)$$

$$\frac{\partial C_{mb}^{-}}{\partial t} = -d_3 B C_{mb}^{-} + d_4 F C_{mf}^{-} + D_{C_{mb}^{-}} \nabla^2 C_{mb}^{-} + w_9. \quad (9)$$

The total negative charge actuators (C_m^-) on the membrane is given by,$C_m^- = C_{mf}^- + C_{mb}^-$. The effect of negative charge actuation on the membrane states is incorporated through a negative feedback term involving C_{mb}^- in the F dynamics as follows:

$$\frac{\partial F}{\partial t} = -(a_1 + a_2 R)F + \left(\frac{a_{30}(1 + U(t - t_s)) + a_3(Z - W)}{a_4^2 + B^2 + a_6 C_{mb}^-} + a_5\right)(F_T - F) + D_F \nabla^2 F + w_F.$$

To mimic the experimental conditions, we reduced the contribution of the polarity mechanism and added an additional term, $U(t - t_s)$ denoting the global agonist stimulation as follows:

$$U(t - t_s) = \frac{a/0.72}{(t - t_s)\sigma\sqrt{2\pi}} \exp\left(-\frac{(ln(t - t_s) - ln\, a - \mu)^2}{2\sigma^2}\right),$$

where t_s denotes the time instant of application of the global stimulation.

For the simulation a 1D domain of length 30 A.U was chosen with periodic boundary condition. The parameter values (in A.U.) used in these simulations are provided in Table S2. With the

central difference approximation of the spatial second derivatives, the coupled SPDEs were converted to a system of coupled stochastic ordinary differential equations (ODE). The stochastic ODEs were numerically solved using Euler-Maruyama method in MATLAB 2019b (MathWorks, Natick, MA, USA) with the aid of the SDE toolbox (http://sdetoolbox.sourceforge.net/) [3]. The time and space discretization steps were chosen to be $\Delta T = 0.001$ A.U. and $\Delta x = 0.1$ A.U. respectively. All the states were restricted to be strictly nonnegative.

References

1. Biswas, D., Devreotes, P. N. & Iglesias, P. A. Three-dimensional stochastic simulation of chemoattractant-mediated excitability in cells. *PLoS Comput. Biol.* **17**, e1008803 (2021).

2. Shi, C., Huang, C. H., Devreotes, P. N. & Iglesias, P. A. Interaction of motility, directional sensing, and polarity modules recreates the behaviors of chemotaxing cells. *PLoS Comput. Biol.* **9**, e1003122 (2013).

3. Picchini, U. SDE Toolbox: Simulation and Estimation of Stochastic Differential Equations with MATLAB. (2007).

Spatiotemporal dynamics of membrane surface charge regulates cell polarity and migration

Tatsat Banerjee[1,2], Debojyoti Biswas[3,†], Dhiman Sankar Pal[1,†], Yuchuan Miao[1,4], Pablo A. Iglesias[1,3], Peter N. Devreotes[1,4,*]

[1]Department of Cell Biology and Center for Cell Dynamics, School of Medicine, Johns Hopkins University, Baltimore, MD, USA.
[2]Department of Chemical and Biomolecular Engineering, Whiting School of Engineering, Johns Hopkins University, Baltimore, MD, USA.
[3]Department of Electrical and Computer Engineering, Whiting School of Engineering, Johns Hopkins University, Baltimore, MD, USA.
[4]Department of Biological Chemistry, School of Medicine, Johns Hopkins University, Baltimore, MD, USA.
[†]These authors contributed equally.
[*]email: pnd@jhmi.edu.

SUPPLEMENTARY NOTE 2

Estimating the amount of resident charges in the inner membrane

Based on existing literature, the inner membrane Zeta potential is usually in the range of -20 to -50 mV. In strict sense, the low potential approximation of the Poisson-Boltzmann equation, is valid for

$$\frac{e\varphi}{k_B T} < 1,$$

where e is the elementary (electron) charge, k_B is the Boltzmann constant and T is the absolute temperature. At room temperature, that means $\varphi \leq 25$ mV. However, as widely accepted in the field, as long as $\varphi \leq 80$ mV, the linearized Poisson-Boltzmann equation offer a close approximation for most applications (1)

We can express surface charge density (charge per unit area), σ, in terms of Zeta potential, φ, using linearized Poisson-Boltzmann equation: φ, is related to the surface charge density (charge per unit area), σ, by

$$\varphi = \frac{\sigma \lambda_D}{\varepsilon \varepsilon_0}, \tag{1}$$

where $\varepsilon \approx 80$ is the dielectric constant of the electrolyte aqueous solution and ε_0 is the electric constant of a vacuum. The quantity $\lambda_D = 1/\kappa$ is the Debye length. For a monovalent electrolyte:

$$\lambda_D = \sqrt{\frac{\varepsilon \varepsilon_0 k_B T}{2 N_A e^2 c_e}}, \tag{2}$$

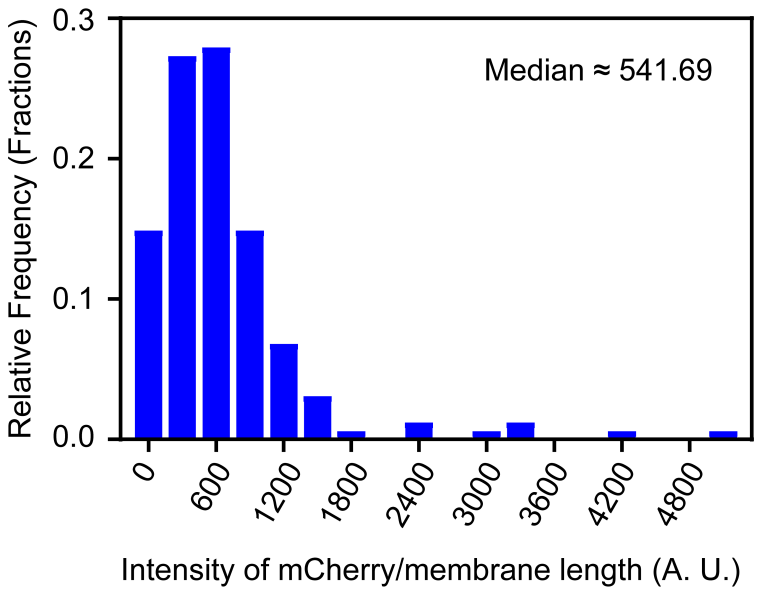

Supplementary Note 2 — Figure 1: Histogram of cAR1-mCherry Intensity. Frequency distribution of cAR1-mCherry intensity is shown in terms of relative fractions. N= 161 cells. Median = 541.7 A.U. The same laser and experimental settings were employed to measure the number of Opto-ACTU+ molecules in the cell.

where e is the elementary (electron) charge, N_A is the Avogadro number and c_e is the molar electrolyte concentration.

Solving in Eq. 2, one gets

$$\lambda_D \approx \frac{0.3}{\sqrt{c_e}}\,\text{nm}. \tag{3}$$

For $c_e = 100\,\text{mM}$, the typical physiological ionic strength, $\lambda_D \approx 1\,\text{nm}$.

Using Eq. 1, considering $\varphi = 35\,\text{mV}$ and accounting for Eq. 3, we get:

$$\sigma \approx 1.5 \times 10^5\,\text{elementary charge} \cdot \mu\text{m}^{-2},$$

which is the amount of resident surface charge density in the inner membrane.

Measuring the amount of charges recruited to the inner membrane

To measure the amount of positive charge recruited to the membrane, we measured the number of Opto-ACTU+ molecules present in the cell, by calibrating it against cAR1-mCherry molecules. From multiple previous radioactive binding assays, it was known that on average number of cAR1 molecules present in the cell is ~60,000 (2, 3). Using a Zeiss 780 confocal microscope, we first recorded the intensity of cAR1-mCherry in 161 different cells and plotted in a histogram (Supplementary Note 2 Figure 1).

Now considering cAR1 molecules were present in a differential shell of thickness Δr, we can write:

$$f \times \frac{I}{h\Delta r} \times 4\pi r^2 \times \Delta r = 60,000\,\text{A.U.}$$

where f is the conversion factor for # of molecules/unit intensity, h is the thickness of the confocal slice (1.2 μm for our confocal settings), and r is the radius of the cell which we can estimate as 5 μm. From there we obtained that for our mCherry fluorophore, $f = 0.423$ molecules/unit intensity.

Next, using exactly the same settings, we imaged cytosolic Opto-ACTU+ molecules where we obtained median fluorescence intensity/unit volume as $\sim$5000 A.U. Thus, total fluorescence intensity of all Opto-ACTU+ molecules in cell would be

$$5000\frac{4\pi r^3}{3} \approx 2.62\times 10^6\,\text{A.U.}$$

which translates into

$$2.62\times 10^6 \times f \approx 1.11\times 10^6\,\text{molecules.}$$

Since each Opto-ACTU+ molecule has charge of $+16$, $\sim$75% of the cytosolic molecules get recruited, and they localize to the back-state region of the membrane, we thus obtained that the recruited charge per unit area of recruitment equals

$$\frac{1.11\times 10^6 \times 0.75 \times 16}{\frac{1}{2}\times 4\pi r^2} \approx 84,800\,\text{charges}\cdot\mu\text{m}^{-2}.$$

This represents around 57% of the estimated resident charge of the membrane under the physiological condition. Replacing this in Eq. 1 suggests that the change in surface potential is of the order of $\varphi_\Delta \approx 19.2\,\text{meV}$.

Effect of recruitment on the firing rate

The reactions in our model of the excitable system (without polarity) are given by:

$$\frac{\mathrm{d}F}{\mathrm{d}t} = -(a_1 + a_2 R)F + \left(\frac{a_{30}}{a_4^2 + B^2} + a_5\right)(F_T - F) \tag{4}$$

$$\frac{\mathrm{d}B}{\mathrm{d}t} = b_1 - b_2 F B \tag{5}$$

$$\frac{\mathrm{d}R}{\mathrm{d}t} = -c_1 R + c_2 F (R_T - R) \tag{6}$$

We assume that the refractory (R) and back (B) equations are at equilibrium, leading to

$$B = \frac{b_1}{b_2 F}, \quad \text{and} \quad R = \frac{c_2 F}{c_1 + c_2 F} R_T$$

and replace these into the equation for the front (F) molecules:

$$\begin{aligned}\frac{\mathrm{d}F}{\mathrm{d}t} &= -\left(a_1 + a_2\left(\tfrac{c_2 F}{c_1 + c_2 F} R_T\right)\right)F + \left(\frac{a_{30}}{a_4^2 + \left(\frac{b_1}{b_2 F}\right)^2} + a_5\right)(F_T - F) \\ &= -\frac{\Big((a_1 c_1 + (a_1 c_2 + a_2 c_2 R_T)F\Big)F\left(a_4^2 b_2^2 F^2 + b_1^2\right) - \Big((a_{30} b_2^2 + a_4^2 a_5 b_2^2)F^2 + a_5 b_1^2\Big)(F_T - F)\Big(c_1 + c_2 F\Big)\Big)}{(c_1 + c_2 F)\left(b_1^2 + a_4^2 b_2^2 F^2\right)}\end{aligned}$$

We can write this as

$$\frac{\mathrm{d}F}{\mathrm{d}t} = -\frac{n(F)}{d(F)}$$

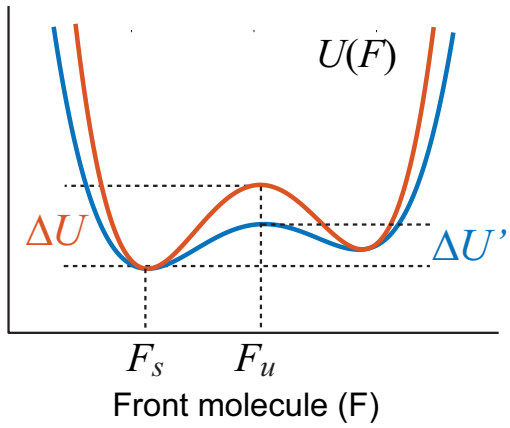

Supplementary Note 2 — Figure 2: Potential function that dictates the firing rate. In this illustration, the system is operating at the stable equilibrium, F_s. In a noise-induced transition, the system moves over the potential barrier onto the other stable equilibrium. The rate at which these transitions can be expected is given by Eq. 7 and depends primarily on the height ΔU relative to the level of noise. Note that small changes in the potential function can lead to large changes in ΔU.

where the numerator is given by a fourth order polynomial in F with coefficients:

$$
\begin{aligned}
n_4 &= \left(a_1 a_4^2 + a_2 a_4^2 R_T + a_{30} + a_4^2 a_5\right) b_2^2 > 0 \\
n_3 &= \left(a_1 a_4^2 + a_{30} + a_4^2 a_5\right) b_2^2 c_1 - (a_{30} + a_4^2 a_5) b_2^2 c_2 F_T \\
n_2 &= (a_1 + a_2 R_T + a_5) b_2^2 c_2 - (a_{30} + a_4^2 a_5) b_2^2 c_1 F_T \\
n_1 &= \left(a_1 + a_5\right) b_1^2 c_1 - a_5 b_1^2 c_2 F_T \\
n_0 &= -a_5 b_1^2 c_1 F_T < 0
\end{aligned}
$$

and the denominator is a cubic polynomial with positive coefficients:

$$
d_3 = a_4^2 b_2^2 c_2, \quad d_2 = a_4^2 b_2^2 c_1, \quad d_1 = b_1^2 c_2, \quad d_0 = b_1^2 c_1.
$$

It follows that any equilibria are given by the roots of the numerator. Because $n_4 > 0$ and $n_0 < 0$, from the law of Descartes, there can either one or three positive roots, with the latter representing a bistable system. The parameters that we use make the complete system excitable, in which case this equation is bistable, with the point of operation at the lower equilibrium. We can integrate this (numerically) to represent the system as:

$$
\frac{\mathrm{d}F}{\mathrm{d}t} = -\frac{\partial U}{\partial F}
$$

where the function U has the shape of a double well potential; see Supplementary Note 2 Figure 2.

In a purely deterministic setting, the system will remain at its equilibrium. In we consider the effect of noise on the system, we consider the Langevin equation

$$
\frac{\mathrm{d}F}{\mathrm{d}t} = -\frac{\partial U}{\partial F} + \sqrt{\sigma}\eta(t)
$$

where the noise is zero mean, and has correlation $\langle \eta(t)\eta(\tau)\rangle = \delta(t-\tau)$. If the system is at one of the stable equilibria (at the basin of the potential well) then a firing will be triggered if the state can move over the

peak because of noise. The rate k at which this occurs is given by Kramers's theory (4, 5):

$$k = \frac{\sqrt{U_s'' |U_u''|}}{2\pi} \exp\Big(-\frac{2\Delta U}{\sigma}\Big) \tag{7}$$

where the terms U_s'' and U_u'' describe the curvature of the potential well at the bottom and top of the potential function, respectively, and $\Delta U = U(F_u) - U(F_s)$ is the height of the barrier. It follows that the main determinant of the rate at which firings are triggered is the height of the well (ΔU) relative to the level of the noise (σ) (6, 7).

We rewrite Eq. 7 as $k = k_0 e^{-\beta \Delta U}$ where $\beta = k_B T$ and consider the effect of changing ΔU by the recruitment of the charge sensors. If we consider the changes in rate from k to $k' = \alpha k$ and assume that the coefficient k_0 is constant between the two, then the change in rates:

$$\alpha = \frac{k'}{k} = \exp\big(-\beta(\Delta U' - \Delta U)\big).$$

If we assume that main determinant of the ΔU is the charge density, we saw above that it is being changed by approximately 19.2 meV and since $k_B T \approx 25.2$ meV, we have that

$$\alpha = \frac{k'}{k} = \exp(19.2/25.2) \approx 2.1$$

which represents a more-than-doubling of the firing rate.

References

1. Butt HJ, Graf K, Kappl M. Physics and chemistry of interfaces. Third, revised and enlarged edition ed. Wiley; 2013.

2. Xiao Z, Zhang N, Murphy DB, Devreotes PN. Dynamic distribution of chemoattractant receptors in living cells during chemotaxis and persistent stimulation. J Cell Biol. 1997;139(2):365–74. doi:10.1083/jcb.139.2.365.

3. Johnson RL, Vaughan RA, Caterina MJ, Van Haastert PJ, Devreotes PN. Overexpression of the cAMP receptor 1 in growing Dictyostelium cells. Biochemistry. 1991;30(28):6982–6. doi:10.1021/bi00242a025.

4. Hänggi P, Talkner P, Borkovec M. Reaction-rate theory: Fifty years after Kramers. Rev Mod Phys. 1990;62(2):251–341. doi:10.1103/RevModPhys.62.251.

5. Kramers HA. Brownian motion in a field of force and the diffusion model of chemical reactions. Physica. 1940;7(4):284–304. doi:10.1016/S0031-8914(40)90098-2.

6. Naoki H, Sakumura Y, Ishii S. Stochastic control of spontaneous signal generation for gradient sensing in chemotaxis. J Theor Biol. 2008;255(2):259–66. doi:10.1016/j.jtbi.2008.08.012.

7. Iglesias PA. Excitable systems in cell motility. IEEE 52nd Annual Conference on Decision and Control. 2013; p. 757–762. doi:10.1109/CDC.2013.6759973.

Spatiotemporal dynamics of membrane surface charge regulates cell polarity and migration

Tatsat Banerjee[1,2], Debojyoti Biswas[3, ‡], Dhiman Sankar Pal[1, ‡], Yuchuan Miao[1,4], Pablo A. Iglesias[3], Peter N. Devreotes[1,4]*.

[1]Department of Cell Biology and Center for Cell Dynamics, School of Medicine, Johns Hopkins University, Baltimore, MD, USA.

[2]Department of Chemical and Biomolecular Engineering, Whiting School of Engineering, Johns Hopkins University, Baltimore, MD, USA.

[3]Department of Electrical and Computer Engineering, Whiting School of Engineering, Johns Hopkins University, Baltimore, MD, USA.

[4]Department of Biological Chemistry, School of Medicine, Johns Hopkins University, Baltimore, MD, USA.

[‡]These authors contributed equally.

*Email: pnd@jhmi.edu.

SUPPLEMENTARY VIDEO LEGENDS

Video S1. Dynamic localization of PI(4,5)P2 to the back-state of the membrane in both *Dictyostelium* and RAW 264.7 macrophages. The spatiotemporal complementary patterns were observed during protrusion formation in *Dictyostelium* (**A**), ventral wave propagation in *Dictyostelium* (**B**), and ventral wave propagation in RAW 264.7 macrophages (**C**). Left panels show $PH_{PLC\delta}$-GFP, middle panels show PH_{Crac}-mCherry (in **A** and **B**) or PH_{Akt}-mCherry (in **C**), and the right panels show the merged view. Top left corners show time in mm:ss format.

Video S2. During ventral wave propagation in *Dictyostelium*, PI(3,4)P2 dynamically localizes to the back-state of the membrane. Left panels show PH_{CynA}-KikGR, middle panels show PH_{crac}-mCherry, and the right panels show the merged view. Top left corners show time in mm:ss format.

Video S3. Dynamic preferential back-state distribution of phosphatidylserine in membrane during ventral wave propagation in *Dictyostelium* and RAW 264.7 macrophages. (A) Ventral wave patterns in *Dictyostelium*. Left panel shows GFP-LactC2, middle panel shows PH_{Crac}-mCherry, and the right panel shows the merged view. **(B)** Ventral wave propagation in RAW 264.7 macrophages. Left panels show overall pattern in the cell; right panels show the pattern in the zoomed-in area corresponding to the white rectangular boxes in the left channel. In either left or right panels, top channels show GFP-LactC2 and bottom channels show PH_{Akt}-mCherry. Scale bar is 10 μm. In both (A) and (B), Top left corners show time in mm:ss format.

Video S4. Dynamic preferential distribution of generic negative surface charge sensor to the back-state of the membrane in *Dictyostelium*. The spatiotemporal patterns were observed during ventral wave propagation (**A**) and protrusion formation (**B**). Left panels show GFP-R(+8)-Pre, middle panels show PH_{crac}-mCherry, and the right panels show the merged view. Top left corners show time in mm:ss format.

Video S5. Dynamic preferential distribution of generic negative surface charge sensor to the back-state of the membrane in ventral waves of RAW 264.7 macrophages. Left panel shows GFP-R(+8)-Pre, middle panel shows PH_{Akt}-mCherry, and the right panel shows the merged view. Top left corners showing time in mm:ss format.

Video S6. Dissociation of PI4P sensor PHOSH2X2 and PI(4,5)P2 sensor PHPLCδ upon recruitment of pseudojanin by chemically induced dimerization system in RAW 264.7 macrophages. (A and B) Left panels: GFP-PHOSH2X2, Right Panels: Pseudojanin. **(C and D)** Left panels: GFP-PHPLCδ, Right Panels: Pseudojanin. All RAW 264.7 cells are expressing Lyn-FRB as well. In all cases, rapamycin addition time was indicated by the appearance of white-colored text "+Rapamycin" in the top middle. Top left corners showing time in mm:ss format.

Video S7. Profile of membrane surface charge sensor R(+8)-Pre, upon recruitment of pseudojanin by chemically induced dimerization system in RAW 264.7 macrophages. (A and B). Two examples of Pseudojanin recruitment in RAW 264.7 cells co-expressing GFP-R(+8)-Pre and Lyn-FRB. Left Panels: GFP-R(+8)-Pre; Right panels: Pseudojanin. Rapamycin addition time was indicated by the appearance of white-colored text "+Rapamycin" in the top middle. Top left corners showing time in mm:ss format.

Video S8. Optically confined recruitment of Opto-ACTU+ can trigger protrusions *de novo*. In (**A-D**), 488 nm laser was selectively irradiated inside the white rectangular boxes; top left corners showing time in seconds; untagged cAR1-CIBN was expressed. (**A and B**) Two examples of Opto-ACTU+ recruitment into the back-state regions of the membrane showing the generation of new protrusions in the vicinity of the recruitment. In (A) stage was moved to start recruitment at time 0s. Left panels: $LimE_{\Delta coil}$ (newly-polymerized F-Actin sensor), right panels: Opto-ACTU+. (**C and D**) Two examples of Opto-CTRL recruitment in the back-states of the membrane, showing no generation of new protrusions from the recruitment areas. Left panels: $LimE_{\Delta coil}$ (newly-polymerized F-Actin sensor), right panels: Opto-CTRL.

Video S9. Global recruitment of Opto-ACTU+ to the membrane in polarized *Dictyostelium* cell elicits random protrusions and abrogates pre-existing polarity and persistent migration. (**A**) Global optical recruitment of Opto-ACTU+. Left panel: Opto-ACTU+, right panel: DIC. (**B**) Global optical recruitment of Opto-CTRL. Left panel: Opto-CTRL, right panel: DIC. For both (A) and (B): Untagged cAR1-CIBN was expressed. Top left corners show time in seconds. The time before recruitment shown with a negative sign. The 488 nm laser was turned

ON at 0s to initiate the recruitment, as depicted by the appearance of green-colored text “488 nm ON” in the bottom middle.

Video S10. Cell morphology and migration mode changes upon global recruitment of Opto-ACTU+ are reversible. (A) and **(B)** demonstrate two examples where Opto-ACTU+ was first recruited to the membrane by turning on 488 nm laser (recruitment initiated when white-colored text “488 nm OFF” switched to green-colored text “488 nm ON” in the videos) which resulted increased protrusion formation, loss of polarity, and impaired migration; then to reverse the process, the laser was turned off (when the green-colored text “488 nm ON” switched to white colored text “488 nm OFF”), Opto-ACTU+ returned to cytosol, and the cell eventually regained its polarized morphology and migration behavior. Left panels: Opto-ACTU+, right panels: DIC; untagged cAR1-CIBN was expressed. Top left corners show time in mm:ss format in (A) and in hh:mm:ss in (B).

Video S11. Cell migration mode and morphology changes in a PTEN– *Dictyostelium* cell, pretreated with PI3K inhibitor LY294002, upon global recruitment of Opto-ACTU+. Left panels show Opto-ACTU+ and right panels show DIC channel. Untagged cAR1-CIBN was expressed. Top left corners show time in mm:ss format. The 488 nm laser was turned ON to initiate the recruitment, as depicted by the appearance of white text “488 nm ON” in the bottom middle.

Video S12. Optically confined recruitment of Opto-ACTU– can locally suppress protrusions in RAW 264.7 macrophages. In both (A)-(C), 488 nm laser was selectively irradiated inside the white rectangular boxes; untagged CIBN-CAAX was expressed; top left corners show time in mm:ss format. Either Opto-ACTU- (A and B) or Opto-CTRL (C) was first locally recruited and then cells were globally stimulated with C5a receptor agonist. The

appearance of white-colored text “+C5aR Agonist” in the videos denoting the addition of the agonist. Left panels: Lifeact-mVenus; Right panels: Opto-ACTU– (A and B) or Opto-CTRL (C).

Video S13. Global recruitment of Opto-ACTU– to the membrane in MCF 10A epithelial cells can deactivate the EGF induced ERK activation. (A) Translocation of ERK-KTR from cytosol to nucleus upon Opto-ACTU- recruitment. Left panel: ERK-KTR-iRFP713, right panel: Opto-ACTU–. (**B**) ERKKTR maintained its cytosolic distribution upon Opto-CTRL recruitment. Left panel: ERK-KTR-iRFP713, right panel: Opto-CTRL. In both (A and B), top left corners showing time in hh:mm:ss format. 488 nm laser was globally turned ON at t=0 (as shown by the appearance of green-colored text “488 nm ON”). Cells were pre-treated with a saturated dose of EGF and they were maintained in that condition throughout the experiment.